Validating Assumptions in Laser Speckle Simulation

2d Lt Aaron Bonner
EENG780 Final Project

Abstract—**This project aims to validate four assumptions made during the development of a laser speckle simulation using data collected from a laboratory experiment. The assumptions addressed in this report are related to the phase screen used, the spatial coherence of the light, the calibration of the photodetector, and the ability to generate speckles at low power.**

Keywords—*laser speckle, spatial coherence, polarization, phase retrieval, photodetector calibration*

I. Introduction

The inspiration for this project is rooted in the theory that it is possible to extract the wavelength of light using laser speckle patterns. Additionally, this idea is set in the context of a optical system embedded in a satellite in space under threat from a ground-based laser or coherent light source. To address this, a laser speckle simulation was developed in previous coursework and treated as a valid system for additional analysis. This report focuses on four assumptions made in the simulation to show that the behavior observed in the generated data is an accurate representation of laser speckles captured by a satellite. These assumptions were then validated using a scientific-grade coherent light source and commercial-grade photodetector in a controlled environment.

II. Laser Speckle Simulation

1. Laser Speckle Simulation

The laser speckle simulation discussed in this project consisted of three major components, the input plane, the aperture plane, and the detector plane. The input plane represents the coherent light entering the system, the aperture plane represents the physical opening of the system and the phase screen, and the detector plane emulates the photodetector of the system. A visual representation of this system is shown in Figure 1.
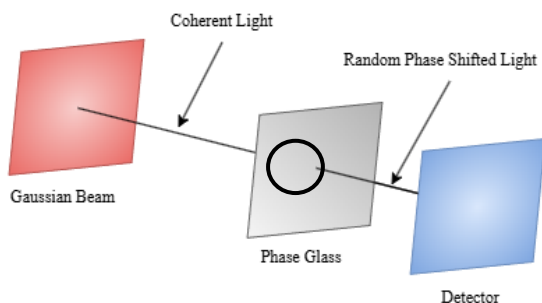

Figure 1. Visual model of the simulation.

The input plane was modeled as a 2D plane wave with a centered Gaussian distribution. The distribution of the plane used a Gaussian distribution as it accurately approximates the real-life behavior of laser beam[1]. The phase of this component was also set to zero to represent a coherent light input. In the simulation, the intensity of the this wave was normalized between zero and one to aid in simplicity.

The aperture plane consisted of two subcomponents. The first component is a random phase screen. This phase screen was modeled as a 2D plane that consisted of uniformly random phase values between zero and two pi. The second component of this plane is an aperture mask. This mask represented the physical opening of the optical system, which in this case was a circular hole. Additionally, at this plane, a scaler factor based on the wavelength of the light used was implemented. Application of this scaler resulted in shorter wavelengths receiving a greater impact on their phase shift compared to longer wavelengths.

The detector plane was not explicitly modeled, but calculated as a result of the propagation of the Gaussian beam through the aperture plane. In the simulation, the intensity field at the detector plane was generated by taking the magnitude of the complex speckle field located at the distance.

The main propagation method used in this simulation was Fraunhofer propagation. Normally, the Fraunhofer propagation would only be valid for long distances due to the need to satisfy the condition that the quadratic phase factor in the Fresnel propagation is approximately equal to one, but it is found that with a lens the far field pattern is found in the lens focal plane [2], which is implemented in the simulation. This propagation is used between the aperture plane and detector plane, with careful calculations in place to ensure that the sampling rate at the detector plane remained the same regardless of the wavelength of the light used during simulation.

The resulting system was then capable of generating speckle patterns between $400nm$ and $700nm$, with an example of a $425nm$ speckle patterns shown in Figure 2.
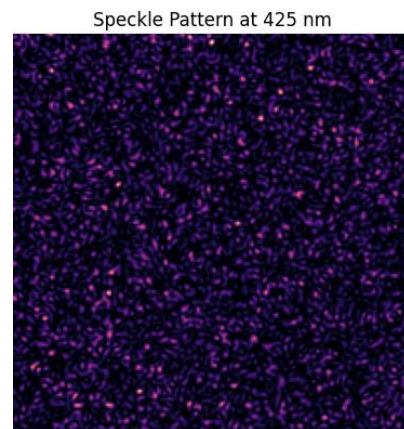

Figure 2. Speckle pattern generated at $425nm$.

2. Assumptions

Throughout the development of this simulation, several assumptions were made, four of which this report seeks to validate. The first assumption is explicitly made during the programmatic implementation of the simulation, and the others are implicitly made in the design and situational context of the simulation. The four assumptions in greater detail are as follows.

A. The phase screen is uniformly randomly distributed

The first assumption pertains to the generation of the phase screen. In the simulation, the phase screen was generated using the $np.random.uniform()$ function. This function is from the NumPy python library and was used to generate a field of uniformly random numbers, which were then multiplied by 2π to transform them to a phase shift. Additionally, the phase screen was divided by the wavelength of the light to better represent the effects that different wavelengths have on a given phase screen. To validate this assumption, phase retrieval was performed on the phase screen used in the laboratory setup.

B. Speckle are accurately generated

The second assumption relates the interaction between a Gaussian beam and a random phase screen. This component was critical to the validity of the system because laser speckles are generated because of coherent light reflecting on or through an optical surface that generates a random interference pattern [3]. To validate this interaction, Young's experiment was performed with the laboratory setup to measure spatial coherence of coherent light source and proven phase screen.

C. Sensor is correctly calibrated

The third assumption demonstrates the importance of photo calibration in a speckle detection system. Although in the system, the sensor represents perfect reading at the detector plane, in real life additional calibration is needed to obtain accurate reading. To validate this assumption, the SANUC and NLS NUC algorithms were implemented to calibrate the laboratory setup and compare power readings.

D. Speckles appear at low power

The fourth assumption incorporates the situational context given for this system, that it is designed to operate in space where laser power from the Earth would be greatly reduced as it propagated though the atmosphere and diverged. To test this assumption, a polarizing filter was used to drastically reduce the power reaching the photodetector.

III. LABORATORY EXPERIMENTATION

All four assumptions discussed were validated using the same general setup, with key components added to adapt the system to different experiments. The laboratory setup consisted of three major components, the coherence light source, the aperture and phase screen, and the photodetector. The detection components of the system were in a self-contained box with a lid to prevent all light from entering, except through the aperture. The size of the box was cube with approximately $10cm$ sides.

The coherent light source used was a Thorlabs Helium Neon (HeNe) laser emitting at $632.8nm$ with a power rating of $5mw$. This laser was placed over a meter away from the detection system, which greatly exceeded the $6cm$ coherence length provided by the manufacturer [4].

The aperture consisted of an approximately $6mm$ hole drilled into the side of the detection box, where a piece of basic office tape was placed on interior of the hole. The tape acted as the phase screen, since it showed a subtle diffusion of spatial coherence when visually observed.

The sensor used was a Raspberry Pi HD Camera. This camera features a 12.3 megapixel sensor with a max resolution of 4056 x 3040 pixels and a pixel size of $1.55\mu m$[5]. For all experiments, the resolution was set to a 2000 x 2000 box. The sensor was located approximately $9cm$ from the inside plane of the aperture and phase screen.
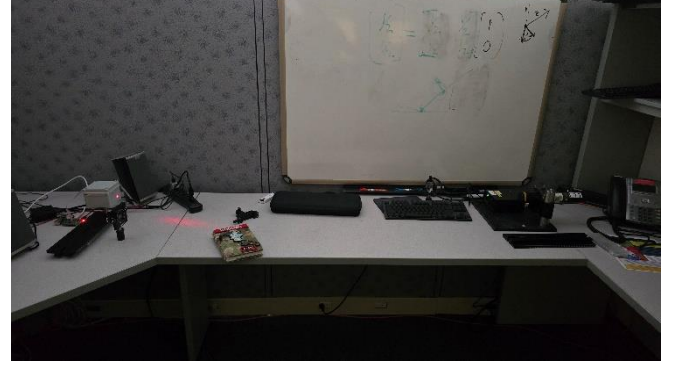
An image of the setup is shown in Figure 3.

Figure 3. The laboratory setup used for validation.

A. Phase Retrieval

The first postulation, which assumed the phase screen was uniformly randomly distributed, was validated using the Gerchberg-Saxton phase retrieval algorithm to recover the phase of the tape.

a) Data Collection

The laboratory setup was first modified to have a $75mm$ located directly at the output of the HeNe laser. The purpose of this lens was to act as a beam spreader to even out the intensity of the laser distribution that exited the laser itself. The beam then propagated though the aperture and phase screen and onto the sensor. The purpose of this adjustment was to ensure that the light entering the aperture had approximately the same intensity and phase, so it could be considered a plane wave impacting the phase screen. During the entire data capture process, a set of five images were captured in short succession, but the following analysis was done on a single image for simplicity. Part of the image used, named $image\_001.jpg$, is seen in Figure 4, cropped from 2000 x 2000 to 400 x 400 pixels for viewing purposes only. The full image was used for calculations.

Figure 4. Cropped image of the speckle captured for phase retrieval.

b) Data Processing and Calculations

Following the initial image collection, several steps were taken to prepare the data for the requirements of Gerchberg-Saxton phase retrieval algorithm.

The first step was to normalize the intensity of the data. After the image was loaded into memory, a dimension test was implemented to check if the data was still in RGB, and if so, it was converted to grayscale. Since the assumption during data collection was that the intensity field was a plane wave at the aperture, by dividing each pixel by the sum of all pixels the data was normalized so that the total intensity summed to one. The amplitude of the normalized intensity was then calculated as the square root of the normalized intensity.

Next, the programmatic implementation of the aperture was implemented. In the experiment, the value of circular aperture was known to be approximately $6mm$. The first consideration for the conversion was that the sampling rate at the detector plane must exactly match the actual sampling rate that the camera had, $1.55\mu m$. The derivation for the sampling rate in the aperture plane, Δx, started with the equation for the sampling rate of the detector plane, Δx_2, seen in Equation (3.1).

$$\Delta x_2 = \frac{\lambda z}{L} \qquad (3.1)$$

In this equation, λ is the wavelength of the light being propagated, z is the distance between the aperture and the detector, and L is the size of the aperture plane. The value for L is the unknown, so it is broken down further using Equation (3.2).

$$L = \Delta x * N \qquad (3.2)$$

In this equation, L is defined as the sampling rate Δx in the aperture plane multiplied by N, the number of values used for the x and y dimensions for the aperture plane. In this case the value of N was 2000 to match the original image dimensions. Rearranging Equation (3.1) to isolate Δx results in Equation (3.3).

$$\Delta x = \frac{\lambda z}{N \Delta x_2} \qquad (3.3)$$

Inserting in the known values for variables on the right-hand side of the equation results in a Δx of $18.37\mu m$. Then, a mesh grid of coordinates is created with X and Y values from $\left[-\frac{N}{2}, \frac{N}{2}\right]$ and separation of Δx. Next, a circle is drawn by programmatically checking the distance between a coordinate and the origin, or center, of the grid. Since the coordinates are a function of the real space Δx, if the distance is less than the radius of the aperture, $3mm$, then that point is inside the aperture.

To verify the validity of the calculations performed, the field was plotted and the aperture size in pixel space was found to span from $X = 837$ to $X = 1163$, resulting in a diameter of 326 pixels. Multiplying this value by the sampling rate Δx calculated earlier results in diameter of $5.988mm$, indicating a successful aperture mask implementation.

The phase screen was expected to follow a uniformly randomly distribution between 0 and 2π, so a 2000 by 2000 grid of random phases between 0 and 2π using $np.random()$. The initial guess was then calculated by performing the Inverse Fourier Transform of the amplitude calculated earlier multiplied by the generated phase screen.

Next, the initial guess was looped through the Gerchberg-Saxton algorithm 100 times. This process is shown in Equation (3.4).

$$\phi_{initial}(x,y) = \text{random}([0, 2\pi])$$

$$A(x,y) = \text{IFT}\left(\text{Amplitude}_{target}(x,y) \cdot e^{j\phi_{initial}(x,y)}\right) \qquad (3.4)$$

Repeat 100 times

$$\begin{bmatrix} B(x,y) = \text{Amplitude}_{source}(x,y) \cdot e^{j \cdot \phi(A(x,y))} \\ C(u,v) = \text{FT}(B(x,y)) \\ D(u,v) = \text{Amplitude}_{target}(u,v) \cdot e^{j \cdot \phi(C(u,v))} \\ A(x,y) = \text{IFT}(D(u,v)) \end{bmatrix}$$

$$\phi_{retrieved}(x,y) = \phi(A(x,y))$$

Following the Gerchberg-Saxton algorithm, the $\phi_{retrieved}$ grid was flattened from 2D to 1D. A histogram of the phase with 200 bins was generated as seen in Figure 5.
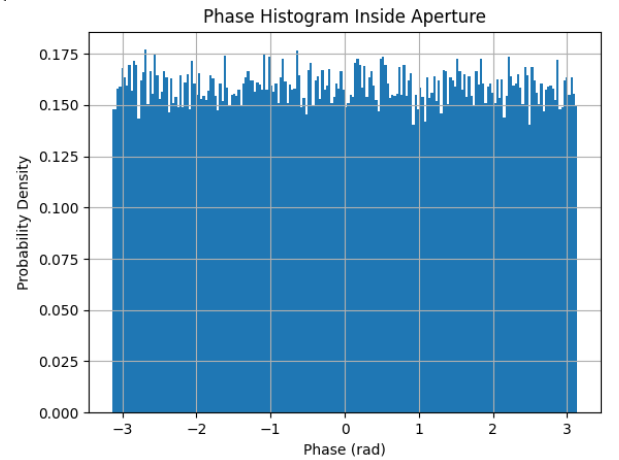

Figure 5. Histogram of the retrieved phases.

Examining this histogram, there is a clear indication that the phases calculated in the phase screen follow a uniformly randomly distribution. This implies that the phase screen adds a spatially random and uncorrelated phase shift to the starting plane wave as it propagates through the aperture. Then, considering each point in the aperture plane as a small random phasor sum, when propagating all the random phasor sums to the intensity plane, a developed speckle pattern is formed as seen in the starting image. This behavior follows the expectation of random phasor sum theory where uniformly randomly distributed phase screens generate speckle patterns. This plot validates the usage of the $np.random.uniform()$ function in the laser speckle simulation.

B. Spatial Coherence

The second postulation, which assumed that the laser speckle patterns were accurately generated via the interaction between a Gaussian beam and a uniformly randomly distributed phase screen, was validated using Young's experiment.

a) Data Collection

Starting from the base setup, a piece of thin cardboard that had two small pinholes punched into it was placed directly in front of the aperture of the detection box. After some physical adjustments, the image shown in Figure 6 was deemed to hold enough interference information to continue analysis.
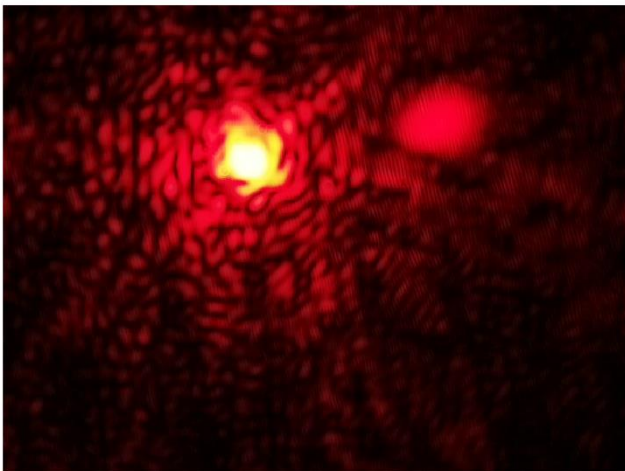

Figure 6. The original full-size image captured by the camera module.

b) Isolating Interference Zone

In the original image, only a small portion of the total capture demonstrated an interference pattern. The zone containing the interference pattern was isolated and the data around it was truncated, resulting in the pattern seen in Figure 7. The location of the zone in the full-size image is in the upper right-hand corner.
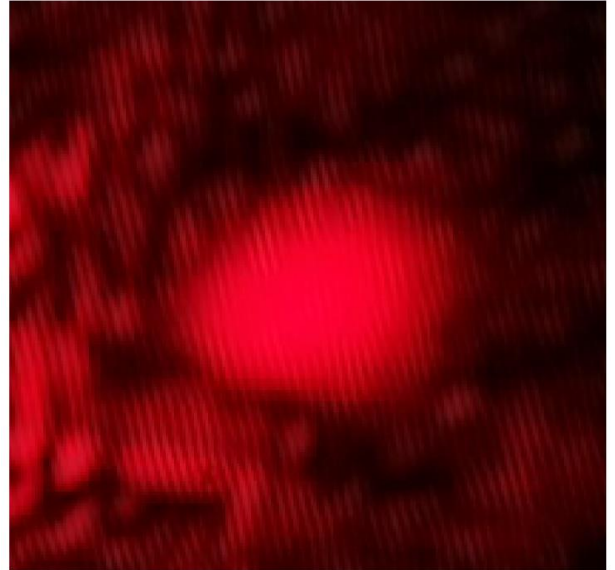

Figure 7. The observed interference pattern.

c) Fringe Pattern Analysis

From the interference region, a horizontal slice of pixels was extracted on a line just below the large dot of saturated data in the center to maximize the number of fringes captured. At this time the data was also converted to gray scale to combine the three colors originally captured with the camera module. The plot of this line is shown in Figure 8.
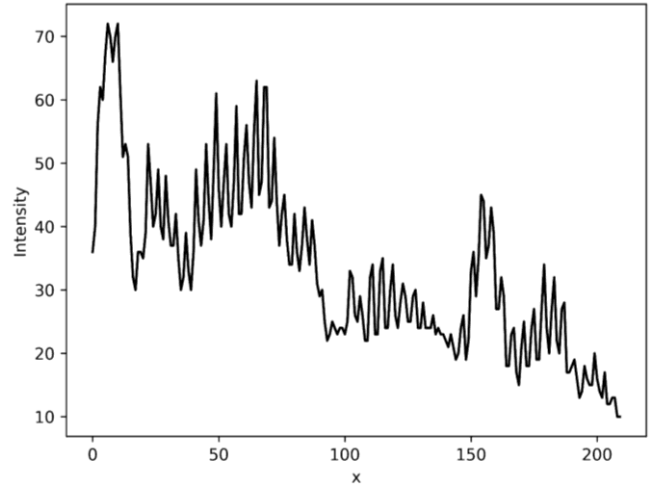

Figure 9. The plot of a horizontal line of data extracted from the interference region.

In this plot, strong indications of uniform peaks and troughs of the intensity were observed, even as the overall underlying intensity fluctuated. To better examine the distance in pixel space between the peaks, the plot was zoomed in, and it was determined that the strongest peak period present was every four pixels. An example of this is shown in Figure 10, where a vertical line is placed at index 45, 49, 53, and 57.
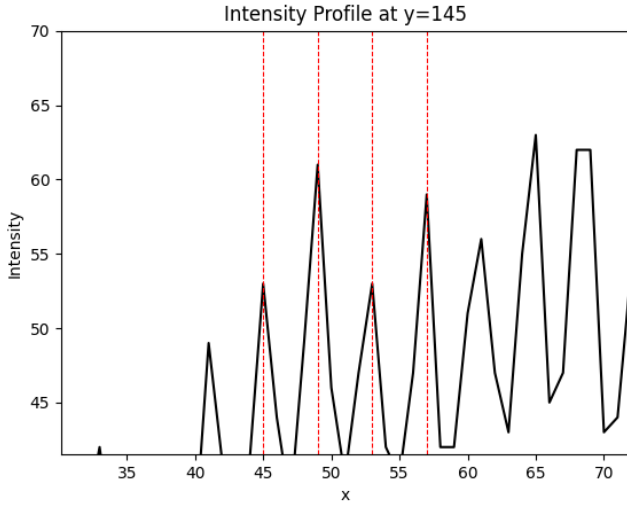
Figure 10. Zoomed in portion of Figure 9 with lines showing four-pixel periodicity.

Considering the pixel size of $1.55\mu m$, it was then determined that the fringe pattern observed exhibited a period of $6.2\mu m$.

At this point, the assumption that a Gaussian beam and a uniformly random phase screen generated spatial coherent speckle patterns was validated. However, another interesting piece of analysis emerged, in that this system could be used to predict the wavelength of other lasers.

d) Application to a Laser of Unknown Wavelength

Given the information known about the laser used to generate the initial data and the hardware parameters of the camera, it then becomes possible to create a model that could be used to derive the wavelength of a new unknown laser, under certain conditions. The model starts with Equation (3.5), the spatial fringe period on the observational plane [6].

$$L = \frac{\bar{\lambda} z}{d} \qquad (3.5)$$

Where L is the spatial fringe period, $\bar{\lambda}$ is the center wavelength, z is the propagation distance from the pinholes to the detector plane, and d is the distance between the pinholes. In this equation, L can be converted to the value Δx, converting the pixel periodicity to a real spacing of $6.2\mu m$ on the sensor. Additionally, considering the center wavelength $\bar{\lambda}$ to be the wavelength of the HeNe laser used to generate the data. Rearranging the equations to consolidate the known and unknown values results in Equation (3.6), the ratio of z to d.

$$\frac{\Delta x}{\lambda} = \frac{z}{d} \qquad (3.6)$$

Inserting in the known values results in a ratio of 9.79772. One strong condition that arrives from this ratio is that any future calculation utilizing it must have the exact same values for z and d to maintain continuity. However, if this condition is satisfied and a laser of unknown wavelength is used to generate new interferences patterns, by performing the same analysis done previously and calculating a new spatial fringe periodicity distance, Δx_2, the wavelength of the unknown laser could be calculated using Equation (3.7).

$$\frac{\Delta x_2}{9.79772} = \lambda_2 \qquad (3.7)$$

C. Photocalibration

The third postulate, which assumed that the detector in the simulation was perfectly calculated, was investigated using the SANUC and NLS algorithms on the laboratory setup. Although the simulation was not designed around accurate power simulation, an alternative was found by estimating the power on the detector in the laboratory setup.

a) Data Collection

Starting from the base system, a polarization lens was first place in front of the aperture and set to be 45° off from the emitted polarization angle of the HeNe laser, reducing it from the estimated $5mw$ to $2.5mw$. Ten images at both one and two millisecond exposure times were then gathered for later calibration calculations. Additionally, another set of ten images at a one millisecond exposure time were captured, but with the lens cover in place to better determine the offset of the camera. A side-by-side image of the first frame of each of the calibration's dataset is shown in Figure 11, clearly showing the differences in intensity.
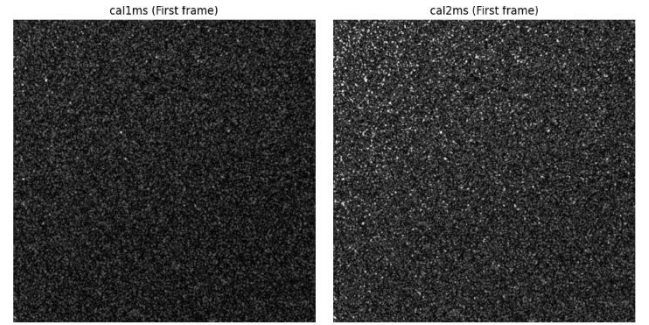

Figure 11. Side by side comparison of the calibration data used.

b) NLS NUC Calibration

To start the NLS NUC calibration process, the offset was found using the average of the offset dataset, resulting in an offset value of one digital count. Next the means of the two calibration sets was calculated. Following this, the estimate $\hat{g}$ was calculated. This estimate is defined by the parameter g, which is shown in Equation (3.8).

$$g(x,y) = \alpha(x,y)K(x,y) \qquad (3.8)$$

Where $\alpha(x,y)$ is the non-linear gain factor of a given pixel and $K(x,y)$ is the number of photons at a given pixel. Solving for the estimate results in Equation (3.9).

$$\hat{g}(x,y) = \arg\min\left(\frac{E[D_2(x,y)-O]}{E[D_1(x,y)-O]} = \frac{(1-e^{-2g(x,y)})}{(1-e^{-g(x,y)})}\right)^2 \qquad (3.9)$$

Where the left side of the internal equation is the ratio of the means of the two datasets, and the right side is the Moment Generating Function of a Poisson random variable. For the programmatic implementation of this calculation, the total number of values required to calculate was four million, and so the process was broken into chunks of ten thousand to prevent computational overload. Following the calculation of $\hat{g}$, the saturation $C(x,y)$ was calculated using Equation (3.10).

$$C(x,y) = \frac{D_1(x,y)-O}{(1-e^{-g(x,y)})} \qquad (3.10)$$

Next, the data was converted from a linear format to a non-linear format using the equations shown in Equation (3.11).

$$H_1 = -\log(1 - (D_1(x,y) - O/C(x,y))$$
$$H_2 = -\log(1 - (D_2(x,y) - O/C(x,y))$$

(3.11)

From the new datasets H_1 and H_2 the means and variances were calculated and the value of $\alpha(x,y)$ was calculated using Equation (3.12).

$$\alpha(x,y) = \frac{\sigma^2_{H_2}(x,y) - \sigma^2_{H_1}(x,y)}{\bar{H}_2(x,y) - \bar{H}_1(x,y)}$$

(3.12)

Following the calculation of $\alpha(x,y)$, the estimate for the number of photons in the $1ms$ dataset was found using Equation (3.13).

$$K(x,y) = \frac{H_1(x,y)}{\alpha(x,y)}$$

(3.13)

The values of $K(x,y)$ where then summed, resulting in a calculated photon count of 300,382,277 for the NLS NUC algorithm.

c) SANUC Calibration

Starting again with the raw datasets, the SANUC calibration algorithm was implemented. First, the mean of the two datasets was calculated with the offset subtracted. Then, the variance was calculated. Next, the linear gain of the detector was calculated with Equation (3.14)

$$G(x,y) = \frac{\sigma^2_{D_2}(x,y) - \sigma^2_{D_1}(x,y)}{\bar{D}_2(x,y) - \bar{D}_1(x,y)}$$

(3.14)

The value of K was then found using Equation (3.15) and the median of $G(x,y)$.

$$K(x,y) = \frac{\bar{D}_2(x,y) - \bar{D}_1(x,y)}{G(x,y)}$$

(3.15)

Similar to the NLS NUC algorithm, the values of $K(x,y)$ were then summed resulting in a photon count of 187,468,908 for the SANUC algorithm.

d) Power Comparison to Estimation

First, an estimation for power reaching the sensor had to be calculated. To do this, the polarization filter was removed from impeding the laser, and the top of the box was opened. Then, using a pair of calipers, the radius of the perceived Gaussian distribution exiting the aperture and falling on the sensor plane was estimated to be $30mm$. Programmatically, a mesh grid of values with a sampling rate of $1.55\mu m$ and height and width of $30mm$ was created. A 2D Gaussian distribution was then overlayed on the grid. The grid was then normalized and multiplied by $2.5 * 10^{-3}$ to convert the grid to milliwatts of power. To calculate the power where the sensor would be, a 2000 x 2000 box in the center was isolated and summed, resulting in a power estimate of $0.019mW$, or 0.74% of the original $2.5mW$. A visualization of this process is shown in Figure 12, with the red box indicating the sensor area.
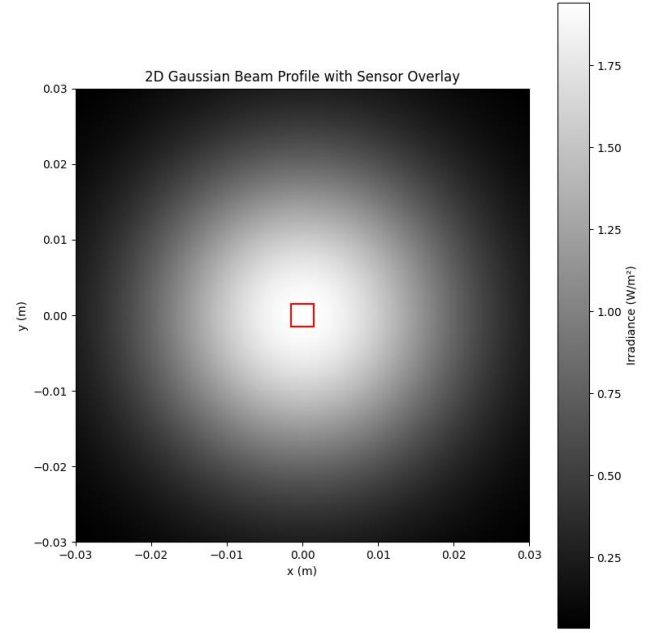

Figure 12. Visualization of the power estimation procedure.

With the number of photons calculated using each photo calibration algorithm, the next step was to calculate the total power on the detector as measured. For this optical system, the size of the sensor was 2000 x 2000 pixels with the size of each pixel being $1.55\mu m$. To convert from photons to power, Equation (3.16) was used.

$$E = \frac{hc}{\lambda}$$

(3.16)

Where h is Plank's Constant, c is the speed of light, and λ is the wavelength of the HeNe laser, $632.8nm$. Following the calculation of the power for the $1ms$ exposure time, the value for both datasets was multiplied by 1000 to get the amount of power in one second. For the NLS NUC algorithm, a power value of $0.094358mW$ was calculated and $0.058889mW$ for SANUC.

Although difficult to validate due to the amount of uncertainty introduced in the calculation of the estimated power, the two calibration methods yielded result within a reasonable margin of error. A more robust way to compare these values would be to use a dedicated power meter at the detector plane. This experiment did not necessarily validate the initial assumption addressed, but started the path to ideal calibration of the real system.

D. Polarization

The last postulation, which assumed that the speckle patterns still appear at low light levels, was validated though the use of a polarization filter.

a) Data Collection

Like the calibration experiment, this experiment used a polarization filter directly in front of the aperture of the detection box.

To find the angle required for low power throughput, the default polarization angle of the HeNe laser was first found. The angle of the 90° offset was first determined, as it was found that at the correct value, the visible light passing through it was nearly zero. An attempt to start from 0° was abandoned as the ability to make visual observations between

polarization degree shifts near the max power was difficult. The result in this testing yielded a 0° polarization angle of 72°, and 90° polarization angle of 162°. The confidence level of the accuracy of these measurements is $\pm 1°$. It is noted that these values are only valid if the HeNe laser remains rotation locked during all trials of the data collection phase.

The exposure time was then increased to $10ms$, as opposed to other experiments that used single digit values. The first data capture attempted used a 88° offset, but the images captured did not show any indicate of speckle patterns. The filter was then turned to an 86° offset, and speckle patterns started to appear. Ten images were captured with a $10ms$ exposure time, and ten more at a $20ms$ exposure time. The offset dataset was reused from the previous experiment, where it showed an offset of one digital count. The first images in the two datasets are shown in Figure 13. The maximum values are also printed.
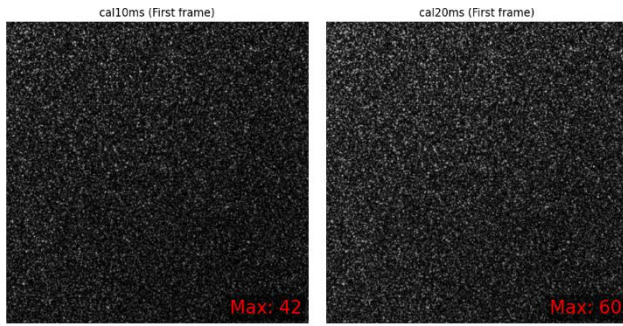

Figure 13. Comparison of the low power speckle patterns

Following the image capture, the SANUC algorithm was implemented to calibrate the detector at this power level. The algorithm calculated a gain of 0.136 digital counts per photon, and total photon count of 120,170,481.

Using the same methodology in the calibration experiment, a total power of $0.003775mW$ was calculated. In comparison to an expected value, from Malus's Law, when linearly polarized light with an intensity of I_0 passes through an ideal polarizer with offset angle θ the output intensity, I, is defined by Equation (3.17).

$$I = I_o \cos^2(\theta) \tag{3.17}$$

For this experiment, if θ is 86°, and the initial power going into the polarization filter is $5mW$, then the expected output would $0.02435mW$. From the photo calibration section, it was found that approximately 0.74% of the light passing through the aperture impacts the sensor. Multiplying the expected power by this factor results in a total estimation of $0.00018mW$ on the sensor itself, an order of magnitude lower than the calculated value. Regardless of the discrepancy, this testing validated the assumption that speckle patterns still appear even at low power levels.

IV. RESULTS

Each assumption made in this project was validated with a varying degree of confidence using a real-life setup and computational analysis.

The first assumption, that the phase screen in the simulation was uniformly randomly distributed, was strongly validated. The histogram of the retrieved phase screen showed clear indication of a uniform distribution, with some variance that was expected. This proved that the usage of the $np.random.uniform()$ function in the simulation would accurately model real phase screens.

The second assumption, that the speckle patterns were accurately generated, was also strongly validated. By adapting Young's experiment to the problem, it was shown that when a coherence beam of light interacted with a validated phase screen, a speckle pattern is formed because of the constructive and deconstructive nature of light at different phases.

The third assumption, regarding the calibration of the sensor and simulation detector plane, was partially validated. Calibrating the real sensor with the SANUC and NLS NUC algorithm resulted in reasonable results, but the lack of a scientific-grade power meter as a reference point made it difficult to assess the validity of the values calculated.

The fourth assumption, hypothesizing that speckle patterns still develop in low power situations, was also validated. Using a polarization filter to attenuate the light to near-zero still resulted in speckle patterns on the sensor. Although the power measured was an order of magnitude off from what was expected based on mathematical calculations, the assumption still holds that speckle is present in low-light conditions.

The results support the overall validity of the initial speckle simulation system and provide experimental justification for four of the assumptions made or implied in its design.

V. FUTURE WORK

While the results of this project provide support for the assumptions made in the simulation, two areas of improvement arose during experimentation.

The first improvement would involve the data capture process. For consistency, during all experiments, the JPEG file format was used, which may have led to unwanted compression. Additionally, the Raspberry Pi camera may have automatically introduced in-camera processing that further degraded signal quality. Transition to a RAW image format and processing the data independently of the camera or capture software would result in greater control and understanding of the capabilities of the camera module.

Additionally, further validation of the SANUC and NLS NUC algorithms could be performed using a dedicated power sensor. This would allow for an accurate comparison of measured power values, as opposed to estimating the field based on visual information. Knowing this information would aid in tuning the camera parameters to accurately detect photons.

These two improvements would further reinforce the experimental validation performed in this report and provide valuable insight into additional work with this optical system.

REFERENCES

[1] Votatera, "Gaussian beam: Propagation, intensity & waist size," Modern Physics Insights: Discover, Understand, Innovate, https://modern-physics.org/gaussian-beam/ (accessed Dec. 13, 2024).

[2] Ghent University Photonics "Fourier Optics," Microphotonics. Available: https://www.photonics.intec.ugent.be/download/ocs130.pdf

[3] F. T. OPTICSTM et al., "Speckle pattern - introduction and applications," AZoOptics,

https://www.azooptics.com/Article.aspx?ArticleID=742 (accessed Dec. 13, 2024).

[4] "Helium-Neon Laser Tutorial."
https://www.thorlabs.com/newgrouppage9.cfm?objectgroup_id=1077

[5] Raspberry Pi Ltd, "Raspberry Pi High Quality Camera," May 2025. [Online]. Available: https://datasheets.raspberrypi.com/hq-camera/hq-camera-product-brief.pdf

[6] J. W. Goodman, Statistical Optics. John Wiley & Sons, 2015.M. Young, The Technical Writer's Handbook. Mill Valley, CA: University Science, 1989.